

Electronic Supplementary Information (ESI) for : "Analysis of Bijel Formation Dynamics During Solvent Transfer-Induced Phase Separation Using Phase-Field Simulations"

Jesse M. Steenhoff ^{*1} and Martin. F. Haase ^{†1}

¹Van 't Hoff Laboratory for Physical and Colloid Chemistry, Utrecht University

In this ESI, additional information is provided on the phase-field simulations presented in the main document, along with associated analysis methods. S0 provides a concise description of the phase-field model and its numerical implementation, while S1 contains a detailed overview of the simulation parameters, organised per Results section. In S2, the calculation procedure for the interfacial tension is explained and discussed. S3 gives supplementary results from phase-field simulations to support certain statements made in the main document. Finally, S4 briefly summarises the analysis method for obtaining the pore size profiles in both experimental and simulated bijel morphologies.

S0: Model description

As a preamble to this section, a list with the nomenclature of the relevant simulation parameters is shown in Table 1.

Table 1: Nomenclature of some relevant simulation parameters

Symbol	Meaning
ϕ	Volume fraction (oil)
ϕ_0	Initial volume fraction (oil)
ϕ_s	Volume fraction (solvent)
ϕ_{sc}	Volume fraction at critical point (solvent)
χ	Interaction parameter (oil-water)
χ_0	Interaction parameter (oil-water, no solvent)
χ_{sc}	Interaction parameter at critical point
\hat{M}	Dimensionless mobility (oil)
$\hat{\kappa}$	Dimensionless gradient energy coefficient
Ψ	Dimensionless free energy density
\hat{t}	Dimensionless time
$\Delta\hat{t}$	Simulation time-step
N	Total simulation steps
\hat{y}	Dimensionless vertical position
$\Delta\hat{y}$	Vertical lattice spacing
σ	Dimensionless interfacial tension
σ_c	Critical interfacial tension

In the main document, the nondimensionalised equations

$$\frac{\partial\phi}{\partial\hat{t}} = \hat{M}\hat{\nabla}^2\left(\frac{\partial\Psi}{\partial\phi} - \hat{\kappa}\hat{\nabla}^2\phi\right) \quad (1)$$

$$\frac{\partial\phi_s}{\partial\hat{t}} = \hat{\nabla}^2\phi_s \quad (2)$$

were solved via finite difference methods on a 200x200 regular square lattice. Spatial discretisation occurred via a centred finite difference with a 5-point stencil, whereas the forward Euler method was used for temporal discretisation.

^{*}j.m.steenhoff@uu.nl

[†]m.f.haase@uu.nl

For a regular solution, the dimensionless free energy density Ψ in Eq. (1) is given by

$$\Psi = \phi \ln \phi + (1 - \phi) \ln(1 - \phi) + \chi \phi(1 - \phi) \quad (3)$$

which couples the phase separation of Eq. (1) to the solvent diffusion of Eq. (2) through the oil-water interaction parameter χ

$$\chi(\phi_s) = \chi_0 - (\chi_0 - \chi_c) \frac{\phi_s}{\phi_{sc}}. \quad (4)$$

With $\chi_{sc} = 2.0$ being set by the regular solution model, choosing $\chi_0 = 3.0$ and $\phi_{sc} = 0.50$ places the critical point in the associated ϕ/ϕ_s phase diagram at the composition $\phi = 0.50/\phi_s = 0.50$, qualitatively mimicking the phase diagram of a well-known STriPS precursor mixture (diethyl phthalate/water/1-propanol). Following the experimental STriPS procedure, simulations (except for section 4.1) were initiated with this critical composition. To reflect the presence of small, thermal inhomogeneities in the composition, the initial state of the system was seeded with random noise uniformly sampled from an $[-0.01, 0.01]$ interval. As such, the initial composition of the simulations is given by $\phi_0 = 0.50 \pm 0.01$ and $\phi_s = 0.50$.

Boundary conditions

For the results presented in the main manuscript, Eq. (1) and Eq. (2) are numerically solved with a variety of different boundary conditions. While these boundary conditions vary per section, and can also differ between Eq. (1) and Eq. (2), they all are enforced through the second order spatial derivative. Therefore, the boundary conditions imposed on Eq. (1) and Eq. (2) in this work can all be classified as so-called (higher-order) "Neumann boundary conditions". Depending on the implementation, the text in the main manuscript distinguishes between "periodic" and "Neumann" boundary conditions. The differences between these categories, as well as the specific implementations for Eq. (1) and Eq. (2), are best illustrated with an example.

With a centred finite difference for the spatial discretisation, the second order derivative of ϕ with respect to the vertical position \hat{y} is approximated via

$$\frac{\partial^2 \phi(\hat{y})}{\partial \hat{y}^2} \approx \frac{\phi(\hat{y} + \Delta\hat{y}) + \phi(\hat{y} - \Delta\hat{y}) - 2\phi(\hat{y})}{(\Delta\hat{y})^2} \quad (5)$$

At the upper boundary of the simulation domain ($\hat{y} = 0$), boundary conditions can be incorporated into the expression of this second order derivative

$$\left. \frac{\partial^2 \phi}{\partial \hat{y}^2} \right|_{\hat{y}=0} \approx \frac{\phi(\Delta\hat{y}) + \phi(-\Delta\hat{y}) - 2\phi(0)}{(\Delta\hat{y})^2} \quad (6)$$

In particular, boundary conditions can be imposed through modification of the value of $\phi(-\Delta\hat{y})$, which represents a virtual lattice point located directly above the upper boundary. For a "periodic" boundary condition, this virtual lattice point is shifted to the bottom boundary of the simulation domain. In a lattice with N_y vertical points, this condition thus imposes $\phi(-\Delta\hat{y}) = \phi([N_y - 1]\Delta\hat{y})$ and consequently

$$\left. \frac{\partial^2 \phi}{\partial \hat{y}^2} \right|_{\hat{y}=0} \approx \frac{\phi(\Delta\hat{y}) + \phi([N_y - 1]\Delta\hat{y}) - 2\phi(0)}{(\Delta\hat{y})^2} \quad (7)$$

In contrast, a "Neumann" boundary condition imposes a certain flux over the upper boundary. Both the oil/water and the solvent can be prevented from leaving the simulation domain by enforcing a situation with zero flux in the respective component over the boundary. This "zero flux" condition is achieved by setting $\phi(-\Delta\hat{y}) = \phi(0)$ and therefore

$$\left. \frac{\partial^2 \phi}{\partial \hat{y}^2} \right|_{\hat{y}=0} \approx \frac{\phi(\Delta\hat{y}) - \phi(0)}{(\Delta\hat{y})^2} \quad (8)$$

Alternatively, the removal of solvent from the simulation domain is achieved by allowing a non-zero flux of solvent over the upper boundary. The extent of this flux is controlled by the value of ϕ_s^{BC} , representing a constant solvent fraction outside the simulation domain. Consequently, $\phi_s(-\Delta\hat{y}) = \phi_s^{BC}$ and the boundary condition becomes

$$\left. \frac{\partial^2 \phi_s}{\partial \hat{y}^2} \right|_{\hat{y}=0} \approx \frac{\phi_s(\Delta\hat{y}) + \phi_s^{BC} - 2\phi_s(0)}{(\Delta\hat{y})^2} \quad (9)$$

For the simulations presented in the main document, "periodic" boundary conditions were used to solve the Cahn-Hilliard equation (Eq.(1)) in section 4.1. For the simulation of the STriPS process, both "flux" and "zero flux" boundary conditions were used to model the solvent diffusion via Eq. (2), representing the presence of either an ambient phase or a solid substrate. In these cases, phase separation was modelled by solving the Cahn-Hilliard equation with "zero flux" boundary conditions. Consequently, for these simulations exchange with the ambient phase is limited to the solvent fraction ϕ_s only.

S1: Simulation parameters

Model validation

For the validation of the phase-field model, as described in section 4.1 of the main document, the initial composition ϕ_0/ϕ_s is varied over the different regions in the ϕ/ϕ_s phase diagram. The chosen compositions, along with the corresponding value of χ (in accordance with Eq. (4)), are listed in Table 2. Additionally, the table lists the binodal compositions ϕ_{bin} that were used for the creation of compositional nuclei in the metastable region of the phase diagram. For all simulations in this region, 75 of such nuclei were placed.

Table 2: Initial precursor compositions for the validation of the phase-field model. Note that only the compositions on the oil-poor side of the phase diagram are listed ($\phi \leq 0.50$). For the oil-rich side, the compositions can simply be calculated by making use of the symmetry of the phase diagram ($\phi' = 1 - \phi$). All simulations were performed with $\hat{M} = 1$ and $\hat{\kappa} = 1$ for $\Delta\hat{t} = 0.01$

χ	ϕ_s	$\phi_0 (\pm 0.01)$	ϕ_{bin}
2.1	0.45	0.25/0.35/0.45/0.50	0.69
2.2	0.40	0.18/0.30/0.40/0.50	0.75
2.4	0.30	0.13/0.25/0.35/0.45/0.50	0.83
2.6	0.20	0.08/0.20/0.30/0.40/0.50	0.88
2.8	0.10	0.05/0.15/0.30/0.40/0.50	0.91
3.0	0	0.03/0.15/0.30/0.40/0.50	0.93

Simulation of STRIPS

Table 3: Relevant simulation parameters for the described phase-field modelling of the STRIPS process, listed per section of the main document Results. Any (-) entry indicates an extension of the value listed earlier in the column.

Section	\hat{M}	$\hat{\kappa}$	σ_c	ϕ_s^{BC}	$\Delta\hat{t}$	N
4.2	0.01	0.50	1.00	0	0.50	30000
4.3	0.01	0.50	1.00	-	0.50	40000
	-	1.00	1.21	-	-	-
	-	1.50	1.38	-	-	-
	0.05	0.50	0.69	-	0.25	80000
	-	1.00	0.70	-	-	-
	-	1.50	0.70	-	-	-
	0.50	0.50	0.30	-	0.02	800000
	-	1.00	0.30	-	-	-
	-	1.50	0.30	-	-	-
4.4	0.01	0.50	0.25	-	0.25	80000
	-	-	0.50	-	-	-
	-	-	0.75	-	-	-
	-	-	1.00	-	-	-
	-	-	1.25	-	-	-
	-	-	1.50	-	-	-
	-	-	1.75	-	-	-
4.5	0.01	0.50	1.00	0	0.50	25000
	-	-	-	0.10	-	-
	-	-	-	0.20	-	-
	-	-	-	0.30	-	-
	-	-	-	0.40	-	-

For the simulation of the STRIPS process, covered in sections 4.2-4.5 of the main document, the relevant simulation parameters are listed in Table 3. In these simulations, phase separation is arrested when the calculated interfacial tension σ exceeds the critical value σ_c . This is achieved by locally multiplying the relative mobility \hat{M} with a factor 10^{-6} in every region where the condition $\sigma \geq \sigma_c$ is met.

As can be seen in the Table, the specific value of σ_c varies between simulations, being mainly dependent on the relative mobility \hat{M} and the gradient energy coefficient $\hat{\kappa}$. Specifically, σ_c is determined based on profiles of the average interfacial

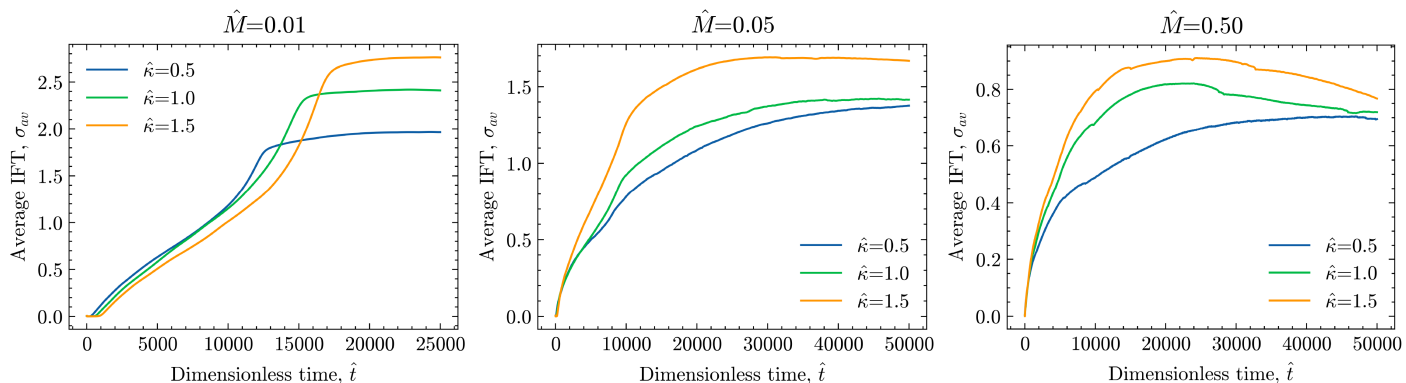


Figure 1: Profiles of the average interfacial tension (IFT) σ_{av} over the course of the STriPS simulation for different combinations of the relative mobility \hat{M} and gradient energy coefficient $\hat{\kappa}$. The onset and subsequent progression of phase separation throughout the system causes an increase in σ_{av} . This increase eventually tapers off, with σ_{av} reaching a somewhat constant value. This is consistent with the separated phases reaching their equilibrium compositions throughout the entire simulation domain.

tension σ_{av} over the course of the STriPS simulation. These profiles, calculated for different combinations of \hat{M} and $\hat{\kappa}$, are depicted in Figure 1.

As can be seen from the profiles, the onset of phase separation induces an increase in the average interfacial tension σ_{av} . As phase separation progresses through the system, the average interfacial tension increases. Eventually, phase separation will have occurred throughout the entire system, quickly followed by the formed phases reaching their equilibrium compositions. Accordingly, σ_{av} plateaus, reaching a somewhat constant value. The height of this σ_c plateau generally increases with $\hat{\kappa}$, consistent with a stronger energy penalty for interface formation.

The values of σ_c listed in Table 3 are based on the plateau value of σ_{av} . In particular, an initial value of σ_c was chosen as half of the plateau σ_{av} . In case this did not result in the arrest of phase separation over the entire system (i.e. locally σ did not reach this value everywhere), the value of σ_c was systematically lowered. The listed values in Table 3 are the maximum σ_c where full arrest of phase separation consistently occurred over the entire simulation domain.

S2: Calculation of the interfacial tension

As mentioned in S1, the simulations of the STriPS process presented in the main document require the continuous calculation of the interfacial tension σ . For a 1D interface, this interfacial tension can be readily calculated in accordance with

$$\sigma_x = \kappa \int_{-\infty}^{\infty} dx \left[\frac{\partial \phi}{\partial x} \right]^2 \quad (10)$$

The relation between the interfacial tension from Eq. (10) and the interaction parameter χ (and by extension the solvent fraction ϕ_s) becomes readily apparent when considering that Eq. (10) effectively states that $\sigma_x \propto (\Delta\phi)^2/\lambda$, where $\Delta\phi$ is the difference in ϕ over an interface with a width of λ . As illustrated by the equilibrium interfaces plotted in Figure 2A, an increasing value of the interaction parameter χ creates a sharper interface by increasing the difference $\Delta\phi$ whilst decreasing the width λ . Since Eq. (10) indicates that sharper interfaces are associated with a higher interfacial tension, increasing the value of χ thus increases the interfacial tension σ_x .

In the presented model, the solvent fraction ϕ_s is linearly related to the interaction parameter via Eq. (4). Consequently, the found relation between the interaction parameter χ and the interfacial tension σ_x can be directly extended to the solvent fraction ϕ_s . This is illustrated in Figure 2B, showing the interfacial tension of 1D interfaces, calculated via Eq. (10) with $\chi_0 = 3.0$ and $\phi_{sc} = 0.50$, for different values of the solvent fraction ϕ_s . These plots readily demonstrate that decreasing the solvent fraction ϕ_s , as happens during the STriPS process, increases the value of the interfacial tension σ_x . When the value of σ_x exceeds a certain set critical value σ_c , indicated by the red dotted line in Figure 2B, phase separation could be arrested through the irreversible attachment of particles to the interface.

However, as illustrated by the inset of Figure 2A, the 2D simulations presented in the main manuscript generally involve multiple interfaces. Additionally, these interfaces can be over perpendicular directions (\hat{x} and \hat{y}). In these simulations, this is addressed by calculating a local measure of the interfacial tension σ for each lattice point via

$$\sigma = \sqrt{\sigma_x \sigma_y} \quad (11)$$

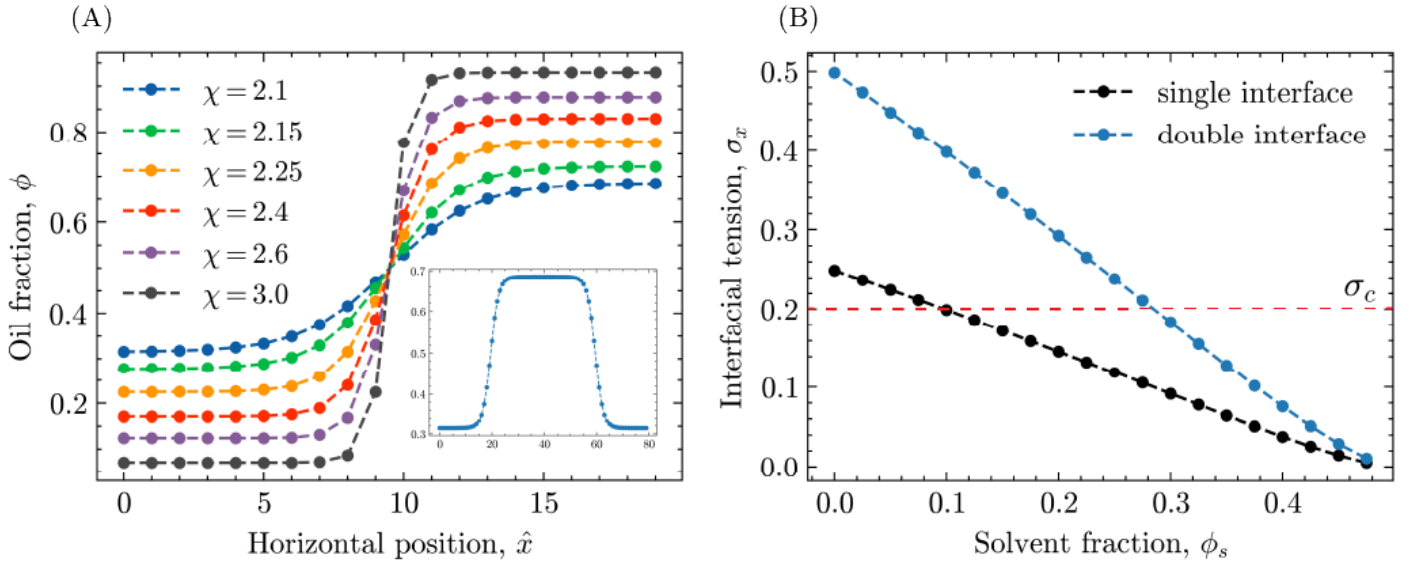


Figure 2: A) Equilibrium shapes of single 1D interfaces in ϕ for different values of the interaction parameter χ . The inset shows a cross-section of an oil-rich domain from a 2D simulation, illustrating the presence of multiple (double) 1D interfaces for a single domain. B) The interfacial tension σ_x , calculated via Eq. (10), over both single and double interface systems for different values of the solvent fraction ϕ_s . The horizontal, dotted red line represents a chosen value of σ_c .

where σ_x and σ_y are obtained in accordance with Eq. (10) through numerical integration over the entire simulation domain in their respective direction. Consequently, the calculated measure σ does not reflect the interfacial tension of a single interface, but rather is a composite measure that has contributions from multiple interfaces in multiple directions. However, as illustrated by the plot of the "double interface" case in Figure 2B, the behaviour of σ for multiple interfaces with respect to ϕ_s is qualitatively similar to that of the "single interface". To obtain equivalent behaviour in terms of arresting phase separation, only a different value of σ_c is required. This calculation method does have the condition, however, that the moment of arresting phase separation can not be unambiguously assigned to a single value of ϕ_s , as the instant where $\sigma \geq \sigma_c$ becomes dependent on local conditions. Theoretically, this could be corrected for by separating and averaging the contributions from the individual interfaces, but this is outside the scope of the current work.

S3: Supplementary simulation results

Boundary layer formation

In the main document, it is stated that the minimisation of gradient energy induces the formation of boundary layers between regions of different composition. This principle is illustrated in Figure 3, showing the progress of phase separation in systems that contain distinct domains of varying composition. For Figure 3A, a circular domain of composition $\phi = 0.52$ is placed in a system with average composition $\phi = 0.50 \pm 0.01$. For Figure 3B, the system contains rectangular domains with respective compositions of $\phi = 0.48 \pm 0.01$, $\phi = 0.50 \pm 0.01$ and $\phi = 0.52 \pm 0.01$.

As can be seen in the Figure, both of these systems result in the formation of boundary layers over the course of the simulation. The shape of the boundary layer is dictated by the shape of the interface delineating the regions of different composition. For the circular and rectangular domains of Figures 3A and 3B, this corresponds to the formation of circular and straight boundary layers, respectively.

There is one additional feature of note in the phase separation depicted in Figure 3. Namely, whereas the compositions of the rectangular domains in Figure 3B contain small inhomogeneities (e.g. $\phi = 0.52 \pm 0.01$), the composition of the circular domain in Figure 3A is fully homogeneous ($\phi = 0.52$). Consequently, phase separation in the circular domain of Figure 3A is directed purely by its interface with the rest of the system. This results in the progressive formation of circular layers, finally giving rise to a morphology similar to concentric rings. In contrast, for Figure 3B the influence of the interfaces between the different domains is limited to their direct vicinity, forming linear boundary layers. Further away from the interfaces, phase separation occurs in a relatively isotropic fashion.

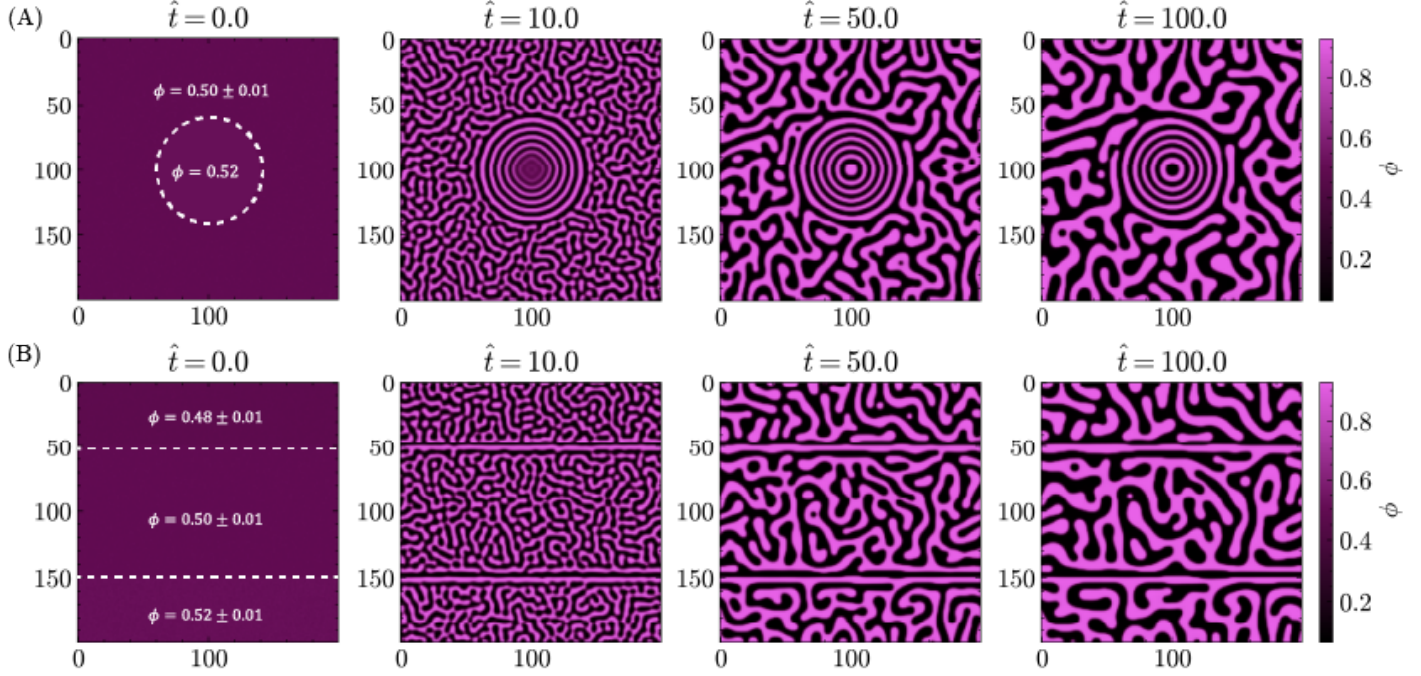


Figure 3: Simulation of phase separation in systems with distinct domains of different compositions. In (A), a circular domain of homogeneous composition $\phi = 0.52$ is placed in a system of composition $\phi = 0.50 \pm 0.01$. In (B), the system consists of rectangular domains with compositions of $\phi = 0.48 \pm 0.01$, $\phi = 0.50 \pm 0.01$ and $\phi = 0.52 \pm 0.01$. All simulations were performed with $\hat{M} = 1$ and $\hat{\kappa} = 1$ for a constant $\chi = 3.0$.

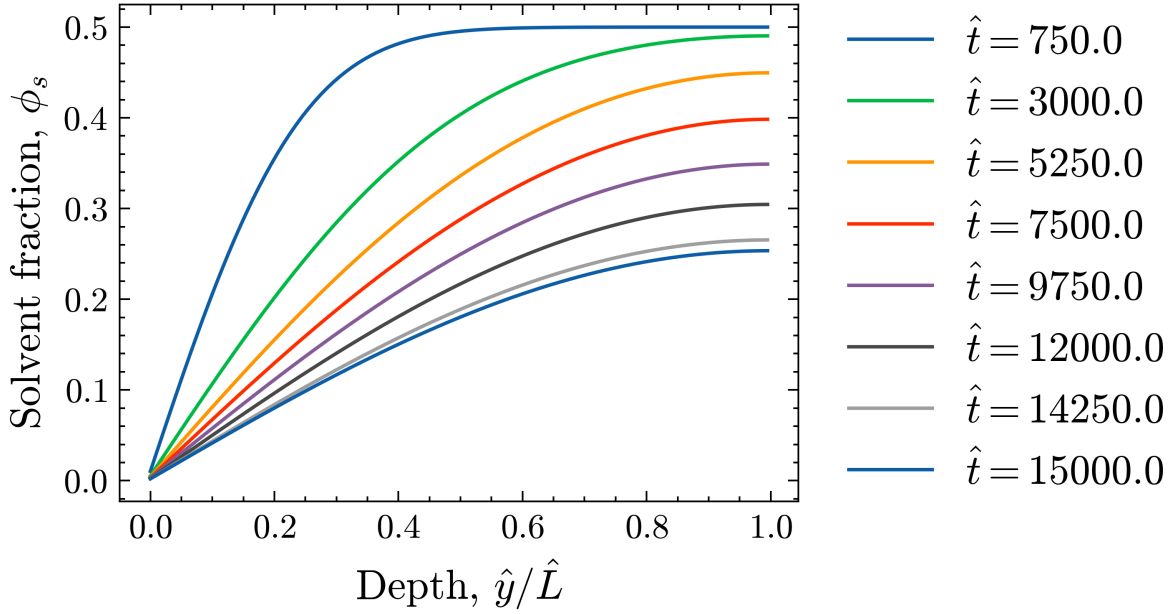


Figure 4: Profiles of the solvent fraction ϕ_s over the simulation domain at different stages of the STRIPS simulation. Here, the interface with the ambient phase is located at $\hat{y}/\hat{L} = 0$, whereas the solid substrate is located at $\hat{y}/\hat{L} = 1$.

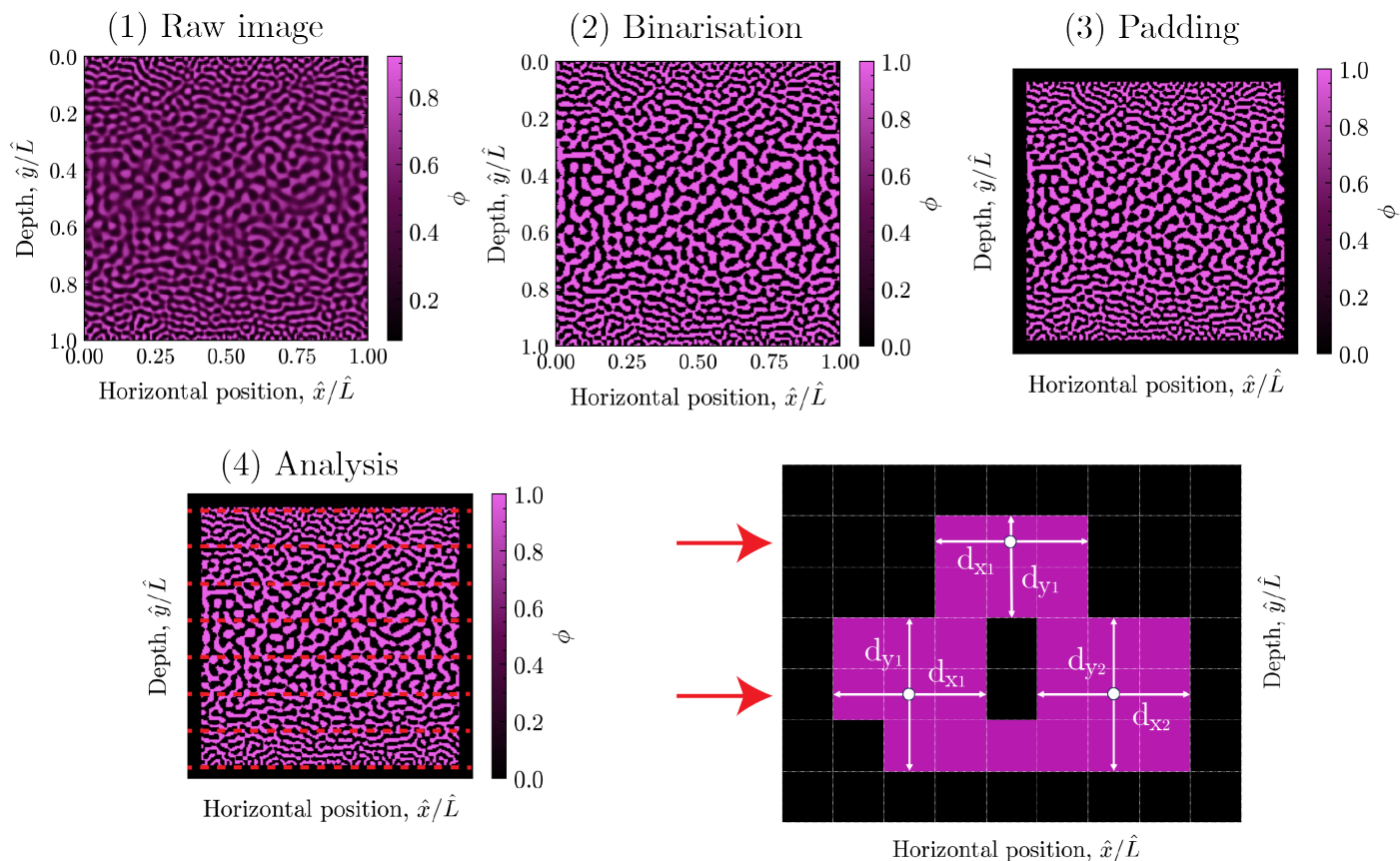


Figure 5: The image-analysis pipeline for calculating the pore size profiles of bijel morphologies. After importing the image as a text file it is binarised and padded. During subsequent analysis, the image is scanned in the horizontal direction at different depths \hat{y}/\hat{L} . Each of these scans finds the total number of pores and their respective perpendicular dimensions \hat{d}_x and \hat{d}_y , in addition to their average \hat{d}_{av} . By taking the mean over all pores in the scan, each depth \hat{y}/\hat{L} can be associated with an average pore dimension \hat{d}_{av} .

Solvent profiles

In the main document, the observed morphologies of STRIPS bijels are explained through the concept of progressive phase separation. This concept is strongly linked with the evolution of the local solvent fraction ϕ_s over the course of the simulation. Therefore, Figure 4 shows profiles of ϕ_s over the simulation domain at different stages of the STRIPS process.

As can be seen in the Figure, the region directly adjacent to the ambient phase ($\hat{y}/\hat{L} = 0$) is quickly depleted of solvent. As such, this region contains a relatively consistent, low level of solvent over the course of the entire simulation. Deeper into the system there are greater gradients in ϕ_s . These gradients are maintained over the course of the simulation, facilitating progressive phase separation. Even deeper, close to the interface with the solid substrate ($\hat{y}/\hat{L} = 1$), the solvent profiles flatten out. Similar to the surface region, the deepest region of the system thus also experiences a relatively homogeneous level of solvent, albeit much higher.

S4: Analysis method for pore size calculations

In the main document, profiles of the average pore size are shown over both the simulated and experimental bijel morphologies. This section briefly describes the analysis method used to calculate these profiles.

Basic principles & Simulated morphologies

The basic principles underlying the used methodology are best explained through an example, here illustrated through the analysis of a simulated bijel morphology. The general pipeline of the analysis process is summarised in Figure 5.

First, an image is imported in the form of a text file. The image is subsequently binarised, generally with a threshold value of $\phi = 0.50$. This is then followed by padding, where the image is artificially extended to prevent any issues caused by overlap between the morphology and the image edges. After this preprocessing, the pore size analysis is performed

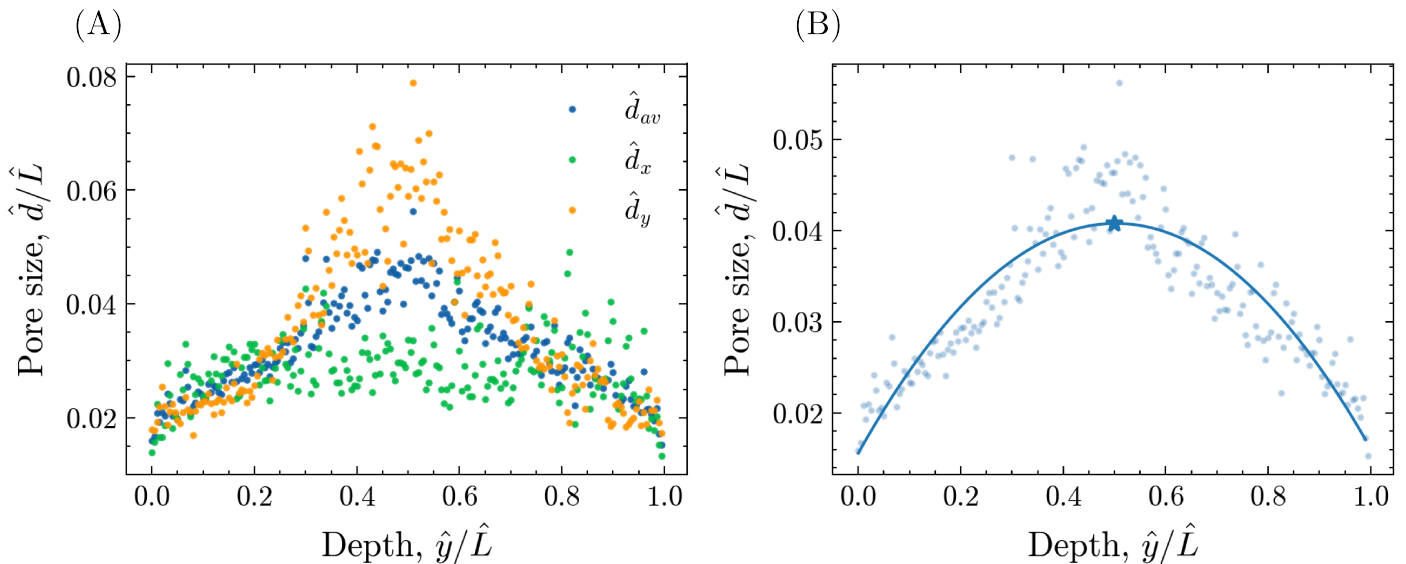


Figure 6: Pore size profiles over the depth of the simulated morphology shown in Figure 5. In (A), the profiles of all three calculated pore dimensions \hat{d}_x , \hat{d}_y and \hat{d}_{av} are depicted. In (B), the profile of the average pore size \hat{d}_{av} is fitted with a quadratic polynomial, with the position of the maximum pore size indicated by the star marker.

over the image. This is done by slicing the image in the horizontal direction \hat{x} at different depths \hat{y} . For each slice, the total number of pores, the lengths of the pores in the horizontal direction d_x and the approximate positions of the pore centres are determined. Starting from the positions of the pore centres, the lengths of the pores in the vertical direction d_y are then calculated. Consequently, each pore has two distinct dimensions associated with it, the perpendicular lengths d_x and d_y . These perpendicular dimensions are then averaged in accordance with

$$d_{av} = \frac{d_x + d_y}{2} \quad (12)$$

The found values of d_{av} are then in turn averaged over all pores in the slice, providing an effective measure for the mean pore dimensions at that depth \hat{y} of the morphology.

After removing the artificial values introduced due to the image padding, the pore size profiles over the morphology can be plotted. This is illustrated in Figure 6, with Figure 6A showing the profiles of the different pore sizes \hat{d}_x , \hat{d}_y and \hat{d}_{av} over the depth of the morphology \hat{y} . Both the pore sizes \hat{d} and the depth \hat{y} are normalised with respect to the total image length \hat{L} . Finally, the profile of the average pore size \hat{d}_{av} is fitted with a quadratic polynomial and the position of the maximum pore size extracted. This is illustrated in Figure 6B, with the position of the maximum pore size indicated by the star marker.

Analysis details for simulated morphologies

In the main document, the pore size profiles of simulated morphologies are presented in sections 4.4 and 4.5. In both these sections, each shown pore size profile is the result of analysing 20 distinct, simulated morphologies that were acquired with the same simulation parameters (except the random seeding of the initial state ϕ_o). The pore size profiles of these 20 morphologies were averaged to yield the shown profile. The fitting of the quadratic polynomials occurred with respect to this average pore size profile.

Finally, for the pore size profiles in section 4.4, a cut-off value of $\phi = 0.525$ was used for binarisation instead of $\phi = 0.50$. Namely, it was found that using $\phi = 0.50$ as the cut-off value did not sufficiently capture the deeper regions of the bijel morphology for higher values of σ_c . For the sake of consistency, all morphologies in section 4.4 were thus analysed with the cut-off value of $\phi = 0.525$.

Experimental morphologies

The pore size analysis of the experimental STRIPS bijel morphologies, acquired via confocal microscopy, is performed similarly to the simulated morphologies, albeit with more extensive image preprocessing.

The pipeline for the analysis of the experimental morphologies is shown in Figure 7. The raw confocal image is first imported into the Fiji ImageJ software and the region of interest isolated. Afterwards, a bandpass filter is applied through the FFT plugin, removing low frequency signal to enhance the image edges. The image is then binarised through

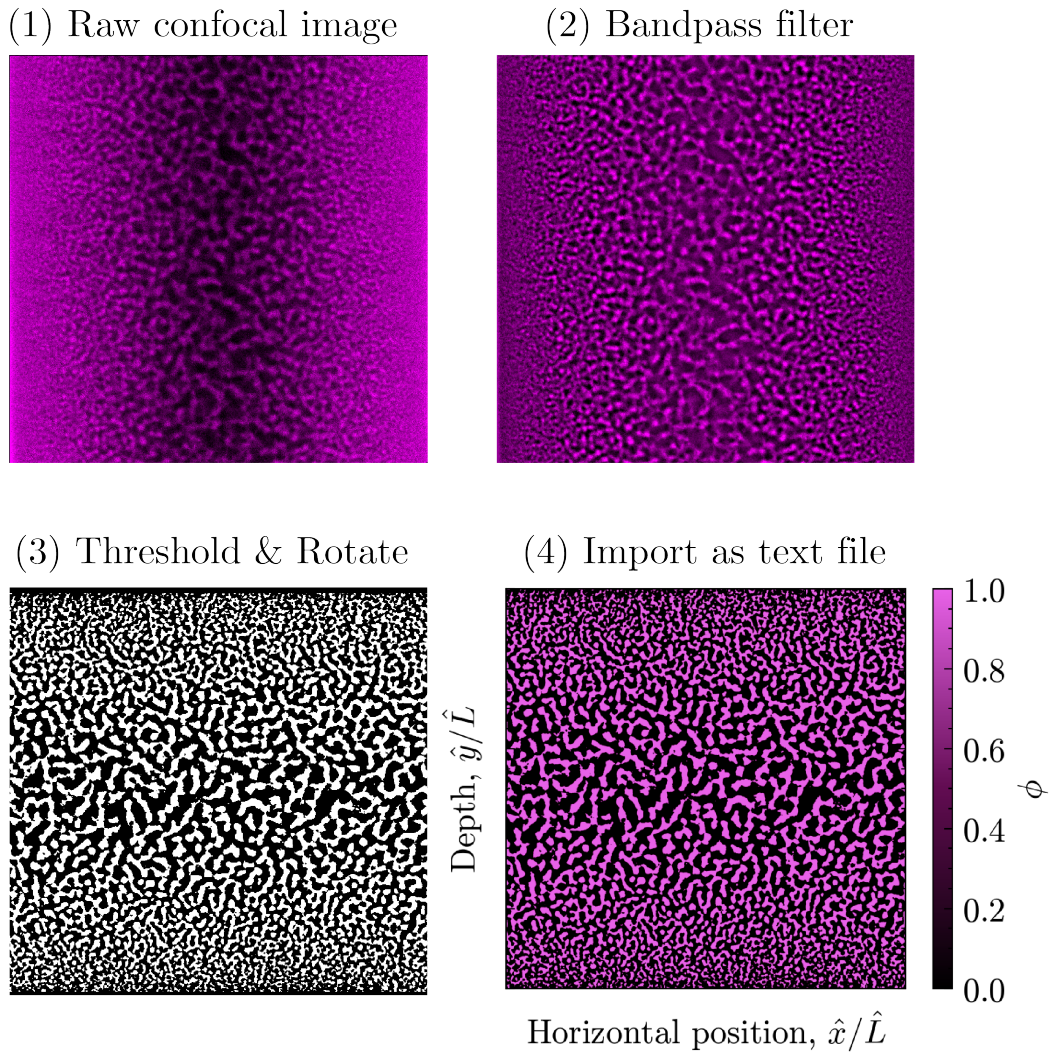


Figure 7: Analysis pipeline for calculating the pore size profiles over experimental STrIPS bijel morphologies from confocal images. First, the raw confocal image is imported into the Fiji ImageJ software and the region of interest isolated. Following the application of a bandpass filter, the image is binarised and rotated such that the interface with the ambient phase aligns with the upper image edge. The resulting image can be exported as a text file, which can subsequently be analysed in a similar manner to the simulated bijel morphologies.

thresholding and rotated in such a manner that an interface with the ambient phase aligns with the upper image edge. Exporting this binarised image as a text file, the experimental morphology can subsequently be analysed analogously to the simulated morphologies, as described in the previous subsection. The results of this analysis, performed for the experimental bijel morphology in Figure 7, are shown in Figure 8.

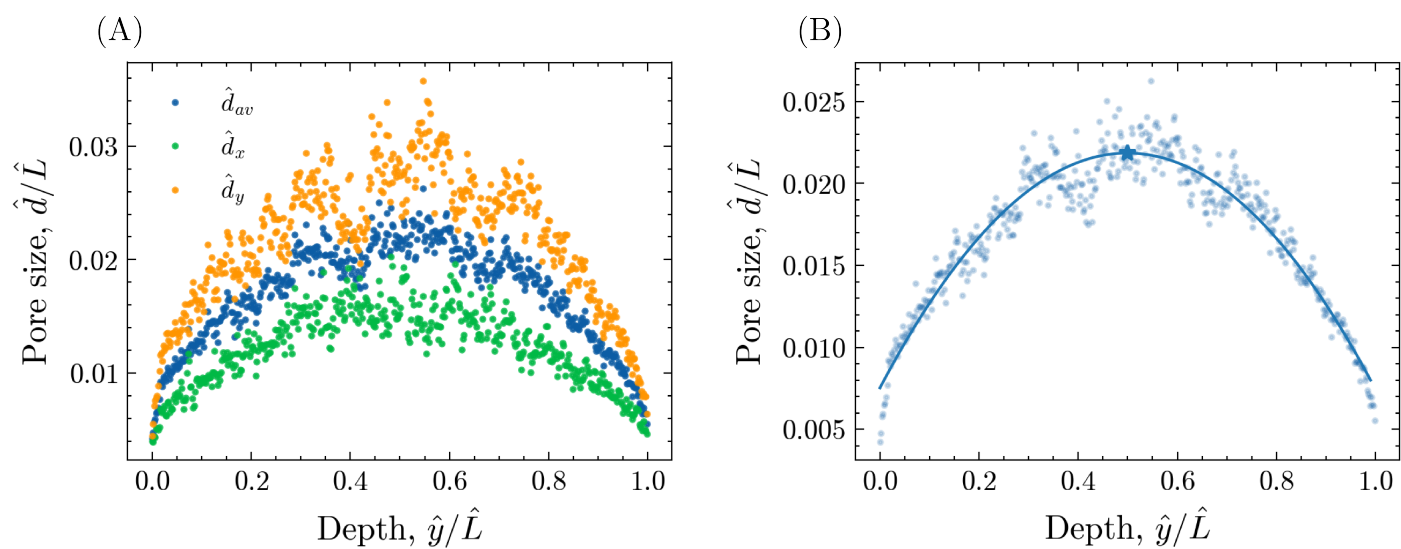


Figure 8: Pore size profiles over the depth of the experimental STRIPS bijel morphology shown in Figure 7. In (A), the profiles of all three calculated pore dimensions \hat{d}_x , \hat{d}_y and \hat{d}_{av} are depicted. In (B), the profile of the average pore size \hat{d}_{av} is fitted with a quadratic polynomial, with the position of the maximum pore size indicated by the star marker.